

Ultrashort Echo Time Magnetic Resonance Fingerprinting (UTE-MRF) for Simultaneous Quantification of Long and Ultrashort T₂ Tissues

Qing Li¹, Xiaozhi Cao¹, Huihui Ye^{1,2}, Congyu Liao¹, Hongjian He¹, and Jianhui Zhong^{1,3}

¹ Center for Brain Imaging Science and Technology, Key Laboratory for Biomedical Engineering of Ministry of Education, College of Biomedical Engineering and Instrumental Science, Zhejiang University, Hangzhou, Zhejiang, China

² State Key Laboratory of Modern Optical Instrumentation, College of Optical Science and Engineering, Zhejiang University, Hangzhou, Zhejiang, China

³ Department of Imaging Sciences, University of Rochester, Rochester, USA

Funding information: This work was supported by National Key R&D Program of China, Grant/Award Numbers: 2017YFC0909200, 2017YFE0104000, 2016YFC1300302; National Natural Science Foundation of China, Grant/Award Numbers: 91632109, 81871428, 61701436, 61525106, U180920013, 81873908; Shenzhen Innovation Funding, Grant/Award Numbers: JCYJ20170818164343304 and JCYJ20170816172431715; Major Scientific Project of Zhejiang Lab, Grant/Award Numbers: 2018DG0ZX01.

Corresponding author: Jianhui Zhong (email: jzhong3@gmail.com) , Room 202A, Zhouyiqing Building, Yuquan Campus, Zhejiang University, No. 38 Zheda Road, Hangzhou, China, 310027.

Submit to *Magnetic Resonance in Medicine* as a *Full Paper*

Word count: 5323

Key words: ultrashort echo time, magnetic resonance fingerprinting, sinusoidal TE variation, bone enhanced image

Abstract

Purpose: To demonstrate an ultrashort echo time magnetic resonance fingerprinting (UTE-MRF) method that allows quantifying relaxation times for muscle and bone in the musculoskeletal system and generating bone enhanced images that mimic CT scans.

Methods: A fast imaging steady-state free precession MRF (FISP-MRF) sequence with half pulse excitation and half projection readout was designed to sample fast T_2 decay signals. Varying echo time (TE) of a sinusoidal pattern was applied to enhance sensitivity for tissues with short and ultrashort T_2 values. The performance of UTE-MRF was evaluated via simulations, phantom and in vivo experiments.

Results: A minimal TE of 0.05 ms was achieved. Simulations indicated the sinusoidal TE sampling increased T_2 quantification accuracy in the cortical bone and tendon but had little impact on long T_2 muscle quantifications. For the rubber phantom, the averaged relaxometries from UTE-MRF ($T_1=162$ ms and $T_2=1.07$ ms) compared well with the gold standard ($T_1=190$ ms and $T_2^*=1.03$ ms). For the long T_2 agarose phantom, the linear regression slope between UTE-MRF and gold standard was 1.07 ($R^2=0.991$) for T_1 and 1.04 ($R^2=0.994$) for T_2 . In vivo experiments showed the detection of the cortical bone (averaged $T_2=1.0$ ms) and Achilles tendon (averaged $T_2=15$ ms). Scalp structures from the bone enhanced image show high similarity with CT.

Conclusion: UTE-MRF with sinusoidal TEs can simultaneously quantify T_1 , T_2 , proton density, and B_0 in long, short, even ultrashort T_2 musculoskeletal structures. Bone enhanced images can be achieved in the brain with UTE-MRF.

Introduction

Magnetic resonance imaging (MRI) provides exquisite contrast in soft tissues. However, bone, tendon, meniscus, and myelin sheath tissues, which have short or ultrashort T_2 values (on the order of 1-10 ms), are barely detectable in conventional MRI (1-3). Ultrashort echo time (UTE) and zero echo time (ZTE) imaging techniques have been used to detect these constituents (4-6). Due to their long scan time, single-point (7,8) and multipoint (9) imaging techniques are rarely used for in vivo studies. To increase k-space coverage efficiency, center-out readout trajectories, such as radial and spiral, are employed (10-12) in association with half-pulse slice selective excitation for 2D imaging or nonselective hard pulse excitation for 3D imaging.

Quantitative UTE imaging has shown extensive applications in diagnosing cartilage degeneration (13), meniscus tears (14), age-related cortical bone deterioration and osteoporosis (15). The cortical bone water concentration, a new metric for the quality of human cortical bone, requires measurements of both T_1 and T_2^* . However, separate acquisitions of T_1 and T_2^* maps typically take more than an hour (1). To reduce the scan time, Abbasi-Rad et al. quantified T_1 using a dual TR method and employed an assumed T_2^* value (15), with obvious omission of T_2^* differences between healthy subjects and patients.

UTE and ZTE techniques are not only applied in MRI systems to diagnose musculoskeletal diseases but also in positron emission tomography (PET)/MRI systems to produce pseudo-CT (pCT) images for PET attenuation correction. Bone contrast is enhanced by suppressing background long T_2 signals using, e.g., a long T_2 suppression pulse (6,16), short T_2 selective double inversion recovery preparation (17), or image subtraction at two echo times (18). Wiesinger et al. obtained pCT images by segmenting the proton density (PD) map using a ZTE sequence (19). Since soft tissue, bone, and air possess different relaxometries and PDs, simultaneous characterization of multiple tissue properties would be beneficial for highlighting bone structures.

Magnetic resonance fingerprinting (MRF) (20), which simultaneously quantifies multiple tissue properties, could benefit the characterization of bone. Different tissue properties such as T_1 , T_2 , T_2^* , and PD are incorporated into the signal evolutions induced by changing the flip angle, repetition time (TR), and echo time (TE) (21). In addition, MRF has shown its potential clinical applications in the human abdomen and brain (22,23). However, challenges remain in using MRF to quantify tissues containing ultrashort T_2 components. First, since the original MRF method has a minimum echo time of several milliseconds, ultrashort T_2 / T_2^* tissues are barely detected. Second, the low proton density in ultrashort T_2 tissue reduces the overall signal and thus degrades the accuracy of MRF dictionary matching. Third, to avoid T_2^* blurring, an acquisition window of $0.81 T_2$ is recommended for 2D imaging (24), which constrains the acquisition window length of cortical bone to submilliseconds. Fourth, since a radial spoke contains less information than a typical spiral arm, several uniformly rotated spokes are needed at each MRF time point (25).

In this work, an ultrashort echo time MR fingerprinting (UTE-MRF) method is proposed to address the problems listed above. The proposed method is based on a fast imaging with steady-state precession (FISP) sequence, which has been demonstrated in previous MRF studies (21,26). In the proposed UTE-MRF sequence, sinc excitation pulses are replaced by self-refocused half pulses (27,28). When combined with the golden angle half-spoke radial projection (29), the minimum echo time is reduced to 0.05 ms. FAs and TEs vary from TR to TR to generate fingerprint-like signal evolutions for long, short, and ultrashort T_2 tissues. Multiple repetitions (reps) are performed to increase the SNR for ultrashort T_2 tissues. Simulations, phantom studies, and in vivo studies were performed to test the proposed UTE-MRF method with respect to tissue quantification and bone enhanced image synthesis.

Methods

Pulse sequence design

A diagram for the 2D UTE-MRF method is shown in Fig. 1 based on the FISP-MRF sequence (26). To reduce the echo time, a 0.7-ms half pulse was employed, which was generated by dividing a 1.2-ms sinc pulse with a time bandwidth of 6 into 2 subpulses. The VERSE algorithm (30) was applied to cool down the peak RF amplitude and the corresponding interrupted slice selection gradient. The half pulses were accompanied by the positive/negative polarized bipolar slice selection gradient to achieve complete slice selection (11,28) and reduce the impact of the eddy current (31). An MRF unit contained 480 images with variable FAs and TEs ($TE_{min} = 0.05$ ms, $TE_{max} = 0.6$ ms, and TE variation period = 120). The FA pattern consisted of four half-period sine waves whose peak FAs were 32° , 22° , 60° , and 10° , and the minimum FA was 5° . TR was fixed at 6 ms.

With ramp sampling, the readout window was 0.79 ms (0.64 ms for the plateau and 0.15 ms for the ramp), and the readout bandwidth was 1780 Hz/pixel. A waiting time of 3 s was applied after MRF unit 1 to recover the spin to its initial state before MRF unit 2. Delay time between MRF repetitions was 3 s. To maximize the SNR while constraining the scan time to less than 1 min, UTE-MRF was repeated 5 times for phantom, ankle, and brain imaging. An additional repetition was performed to increase the SNR for bone quantification, leading to a scan time of 68 s. To increase data incoherence and reduce the eddy current effect within a repetition, the radial spokes were rotated at a small golden angle (23.62°) (29,32). Among repetitions, the radial trajectories were uniformly distributed over a unit circle.

Direct B_0 map estimation from the phase of MRF frames

In previous MRF studies, echo time variations were applied to either increase T_2^* sensitivity (33) or to separate water and fat signals (25,34). In this study, we employed a sinusoidal TE varying pattern to increase MRF sensitivity for short and ultrashort T_2 tissues. Fig. 2 shows the signal evolutions of six tissue constituents (under the same T_1 of 180 ms but increased T_2 values of 0.5, 1, 2, 5, and 10 ms) simulated with the extended phase graph (EPG) (35,36) and FA pattern in Fig. 1b. Intuitively, normalized signal evolutions under constant TEs (first two columns in Fig. 2) are difficult to differentiate, even when TE is minimized to 0.05 ms. Sinusoidal TE sampling (from 0.05 to 2 ms) increases the signal evolution differences. However, variable TE causes a spatially and temporally dependent phase based on field offset and TE. To prevent these phase disturbances, Rieger et al. only used the magnitude of both measured data and dictionary entries (33). To avoid loss of phase information, off-resonance-induced phase error was corrected by either employing a prescanned B_0 map (37), or incorporating the B_0 effects into the MRF dictionary (34). However, these methods add extra computation in MRF dictionary generation and matching processes. To avoid such shortcomings, we adapted a dictionary-free B_0 estimation method based on the sinusoidal TE pattern, an idea inspired by the amplitude modulation and demodulation that has been widely employed in communication systems (38). The phase accumulated in MRF image series is modulated by the field offset B_{off} and sinusoidal TE carrier wave ($\alpha \sin(\omega\tau) + \beta$),

$$Phase = 2\pi i \cdot B_{off} \cdot (\alpha \sin(\omega\tau) + \beta) + n, \quad [1]$$

where B_{off} is the frequency offset (unit: rad) caused by field inhomogeneity and the chemical shift; α , β , and ω are TE sampling parameters, where $\alpha = (TE_{max} - TE_{min})/2$, $\beta = (TE_{max} + TE_{min})/2$, and ω is the frequency of the sinusoidal waveform; τ is the time vector $[1, 2, \dots, F]^T$ (unit: TR); and n represents the noise term. To estimate B_{off} , the accumulated phase in [1] is demodulated via multiplying the carrier wave $\sin(\omega\tau)$,

$$dPhase = (2\pi \cdot B_{off} \cdot (\alpha \sin(\omega\tau) + \beta) + n) \cdot \sin(\omega\tau). \quad [2]$$

$dPhase$ is then derived as

$$dPhase = 2\pi \cdot B_{off} \cdot \alpha \cdot \left(\frac{1+\cos(2\omega\tau)}{2}\right) + (2\pi \cdot B_{off} \cdot \beta + n) \cdot \sin(\omega\tau). \quad [3]$$

The noise term n in [3] comprises physiological, thermal, and other MRI system-related noise. However, since phase maps are reconstructed from single k-space interleaving at each TR, the noise n consists mostly of data undersampling aliasing. To reduce k-space undersampling-induced phase noise, a sliding window matrix S is applied (39) and multiplied from both sides of [3],

$$S \cdot dPhase = 2\pi \cdot S \cdot B_{off} \cdot \alpha \cdot \left(\frac{1-\cos(2\omega\tau)}{2}\right) + S \cdot (2\pi \cdot B_{off} \cdot \beta + n) \cdot \sin(\omega\tau) \quad [4]$$

where S is an $F \times F$ array containing values of either 0 or 1. Each row at S behaves as a window. Only if the element is within the window, its value is 1; otherwise, 0. From the first row to the last row in S , the window moves from left to right. For a sliding window matrix with a window size of 4, we have S in the form of

$$S = \begin{pmatrix} 1 & 1 & 1 & 1 & 0 & \dots & 0 & 0 \\ 0 & 1 & 1 & 1 & 1 & \dots & 0 & 0 \\ 0 & 0 & 1 & 1 & 1 & \dots & 0 & 0 \\ & & & \vdots & & & & \\ 0 & 0 & 0 & 0 & 0 & \dots & 1 & 1 \end{pmatrix}_{F \times F} \quad [5]$$

Due to the nature of the smoothed phase maps (shown in the supplementary video), the noise n shows little impact and is ignored after the sliding window. A time integral among constant TE periods mT ($T = 2\pi/\omega$, and m is the number of periods) is employed as a lowpass filter, such that constant phase accumulations carried by $\cos(2\omega\tau)$ and $\sin(\omega\tau)$ are neutralized. The field offset B_{off} is derived as follows:

$$B_{off} = \frac{2}{2\pi \cdot \alpha \cdot mT} \cdot \sum_0^{mT} (S \cdot dPhase) \quad [6]$$

Image reconstruction

MRF dictionaries were generated under variable FAs in Fig. 1b and sinusoidal TEs ($TE_{min} = 0.05$ ms, $TE_{max} = [0.05:0.05:1.0]$ ms) using EPG. Since our previous work have demonstrated that the TE variation period had little impact on the tissue

quantification (40), the TE variation period was set to 120 TRs. Dictionary T_1 values varied from 10 to 3000 ms, including [10:10:400, 400:20:2000, 2000:40:3000] ms. The T_2 values varied from 0.1 to 300 ms, including [0.1:0.1:5, 5:5:150, 150:10:300] ms. A two-step dictionary generation method was performed to model the partial recovery effect (41,42). The dictionary entries were normalized.

Parametric maps of T_1 , T_2 , PD, and B_0 were generated in four steps. First, multichannel images were transformed from k-space into image space using inverse NUFFT (43) and combined using adaptive coil combination (44). Images from positive and negative excitations were directly complex summed. Second, the B_0 map was estimated from MRF phase maps based on [6], where a sliding window length of 20 was employed to balance the reduction of undersampling aliasing and tissue specificity lost. Meanwhile, phase maps from frame No. 240 to 480 (i.e., 2 TE variation periods) were used to avoid the superposition of IR-induced phase inversion. Third, to remove phase accumulations induced by field inhomogeneity, complex MRF images from step 2 were multiplied by the conjugate phase maps depending on B_0 and TE. Fourth, image frames were normalized and their dot-product with dictionary entries were calculated (20). Since cortical bone has low spin density and ultrashort T_2 , it is sensitive to bone marrow signals from radial undersampling artifacts. Here, we first employed the partial volume dictionary matching method (45) to estimate and remove bone marrow components and then applied MRF dictionary matching to obtain the cortical bone T_2 .

Since an adiabatic IR pulse was utilized, the MRF possessed an intrinsic advantage in long T_2 suppression near the soft tissue IR-null point. Although the ultrashort T_2 relaxation time of bone makes it decay quickly in the transverse plane, it recovers rapidly and shows longitudinal hyperintensity due to its short T_1 . With the calculated T_1 and T_2 maps, transverse and longitudinal magnetization maps at any MRF frame can be generated by reference to the dictionary. The skull enhanced images were obtained by selecting a proper frame in the longitudinal magnetizations where ultrashort T_2 bone was highlighted.

Simulation study

To investigate the impact of the sinusoidal TE sampling on the accuracy of tissue quantification, numerical simulations were carried out on a digital phantom (size of 110 x 110) shown in Fig. 3, including muscle, tendon, total water of bone, and free water of bone. Dark space in the phantom was for air. Most of the tissue properties (listed in Fig. 3b) were chosen following the literature (17,46,47). Ideal MRF frames were generated from MRF transverse magnetizations using EPG. Although the TE variation increased the specificity of the MRF to short T_2 , it introduced a TE-dependent T_2^* weighting. Since the impact of T_2 was modeled into MRF signal evolutions through EPG, the T_2^* -caused decay, $\exp(TE/T_2^*) = \exp(TE/T_2 + TE/T_2')$, was incorporated by multiplying the ideal MRF frames by an additional exponential T_2' decay. The nominal T_2' values, which are shown in Fig. 3b, led to a T_2^* of 25 ms for muscle, 2.3 ms for tendon, 0.7 ms for the total water of bone, and 2.4 ms for the free water of bone.

SNR variations were also considered. Complex white Gaussian noise was added to represent different SNR levels as listed in Fig. 3b. k-Space samples were obtained point-by-point through forward NUFFT of the noised MRF frames, the golden angle rotated radial readout and the corresponding density compensation function (48). TE_{min} was fixed at 0.05 ms, and TE_{max} was increased from 0.05 to 1 ms in steps of 0.05 ms. Multiparametric maps were reconstructed following the method in the image reconstruction section. The root mean square error (RMSE) of the measured T_1 and T_2 maps was calculated compared to the gold standard T_1 and T_2 values.

Phantom and in vivo experiments

Experiments were conducted on a whole-body 3T scanner (Magnetom Prisma, Siemens Healthineers, Erlangen, Germany). A homemade phantom (Fig 5) with agarose tubes (mimicking soft tissues) and rubber plugs (mimicking ultrashort T_2 tissues) was imaged using a 20-ch head coil. Seven of those tubes were filled with different concentrations

of MnCl_2 to represent tissue components of variable T_1 and T_2 values, and one tube was filled with vegetable oil (94% soybean oil and 6% sunflower oil), which has one dominant resonance peak at about 3.46 ppm from water (see Supporting Information Figure S1) similar as Reeder et al. reported (49). In vivo experiments were carried out with the approval of the local institutional review board. A healthy volunteer participated in calf and tendon imaging using a 15-ch knee coil. Brain scans were performed on 3 healthy volunteers and a patient with facial neuromas using a 64-ch brain coil. For the healthy volunteers, the FA trains in Fig. 1a were used. The SAR reported by the scanner was 48% of the safety threshold under Normal mode. For the patient scan, the FAs were halved for safety considerations. The bone enhanced image from the patient was compared with CT images (tube voltage = 80 kV, tube current = 365 mA, DLP = 97.9 mGy·cm, mean dose = 0.34 mSv, slice thickness = 1.0 mm, and resolution = $0.5 \times 0.5 \text{ mm}^2$) acquired and reconstructed on a Philips iCT scanner (Brilliance iCT, Philips Healthcare, The Netherlands) for her surgery planning at a local hospital. The 3D CT images were rotated to match the orientation of the MRI image using the function of 3D volume rendering in RadiAnt Dicom Viewer (Medixant Co., Poland).

The slice thickness was 6 mm for the phantom and 7 mm for the in vivo study. To obtain a high-quality bone enhanced image, TE was minimized to 0.05 ms and was unchanged for the brain scan. Multiparametric maps were reconstructed to achieve a resolution of $1.0 \times 1.0 \text{ mm}^2$ (matrix size of 240×240) for the phantom, leg, and tendon and $0.75 \times 0.75 \text{ mm}^2$ (matrix size of 256×256) for the brain using MATLAB R2014a (The MathWorks, MA) on a Linux (Red Hat Enterprise) server (with Core i7 Intel Xeon 2.8 GHz CPUs and 64 GB RAM).

An inversion recovery UTE (IR-UTE) sequence was used to acquire a gold standard T_1 map with inversion times (TIs) = 50, 100, 200, 400, and 800 ms, TR = 3000 ms, TE = 0.05 ms, and number of spokes = 248. The gold standard T_2^* map was generated from a UTE sequence with TEs = 0.05, 0.2, 0.5, 1, 2, and 4 ms, TR = 1500 ms, and number

of spokes = 248. All images acquired with the IR-UTE and UTE sequences were reconstructed following the first step of MRF image reconstructions. The gold standard T_2 map was measured with a spin echo (SE) sequence with TEs = 25, 50, 75, 100, and 125 ms, TR = 3000 ms, matrix size = 192 x 192, resolution = 1 x 1 mm², and 6/8 partial Fourier acquisition. The total acquisition time was 124 min for T_1 , 74 min for T_2^* , and 36 min for T_2 . T_1 , T_2 , and T_2^* maps were reconstructed using a toolbox (<http://www-mrsrl.stanford.edu/~jbarral/t1map.html>) (50).

Results

Simulation

Fig. 4 shows the simulation results of the musculoskeletal tissue mimic phantom under 3 and 6 MRF reps. Overall, the T_1 and T_2 RMSEs are decreased by approximately twofold with twice repetitions. The T_1 and T_2 quantification of muscle are robust against TE variations. Tendon and bone total water show higher improvement in T_2 quantification with extended TE sampling in 3 reps than in 6 reps. T_1 RMSEs are slightly increased from 33/17/77 ms to 36/21/82 ms for tendon/total water/free water under 6 reps. Free water shows the largest quantification errors due to its lowest PD. When T_1 and T_2 maps reconstructed at $TE_{max} = 0.6$ ms are compared with the gold standard T_1 and T_2 (Fig. 4b), strong streaking artifacts are observed with 3 reps, especially in the T_2 difference map. When the repetitions are increased to 6, T_2 quantification errors are substantially reduced, but T_2 biases are observed in tendon and free water. The average measurements from UTE-MRF under 6 reps with $TE_{max} = 0.6$ ms is compared with nominal relaxometries in Supporting Information Table S1. UTE-MRF shows high-degree agreements with nominal T_1 . However, the T_2 values from UTE-MRF tend towards the nominal T_2^* from the longest T_2 in muscle to the shortest T_2 in bone total water.

Phantom and In Vivo Studies

Fig. 5 shows the phantom quantitative maps from the UTE-MRF and gold standard methods. Since rubber is undetectable in the SE sequence, the gold standard T_2^* is measured instead of T_2 for rubber and compared with the quantified T_2 from UTE-MRF. The T_1 , PD, and T_2 (agarose phantom) maps agree well with the gold standard. Meanwhile, the rubber T_2 measured with UTE-MRF is close to the gold standard T_2^* . The oil T_2 is approximately 120 ms accompanied with a ~ 400 Hz frequency shift detected by UTE-MRF, which is close to the reported value of fat (44), but is underestimated in SE method.

Fig. 6 shows the ROI-based comparisons between UTE-MRF and the gold standard. The T_2 from UTE-MRF is compared with the gold standard T_2^* for the ultrashort T_2 rubber phantoms (red markers) and with the gold standard T_2 for the other long T_2 agarose tubes (green markers). For the long T_2 agarose phantoms the T_1 and T_2 values from UTE-MRF show good agreement with the gold standard T_1 ($y = 1.07x - 43.71$, $R^2=0.991$) and T_2 ($y = 1.04x - 3.27$, $R^2=0.994$). Fig. 6b lists the T_1 and T_2 values of UTE-MRF from the chosen ROIs.

Fig. 7 shows in vivo ankle and leg results from UTE-MRF. Since T_2 varies from several microseconds in bone to one hundred or more microseconds in bone marrow, the T_2 maps are displayed separately on two scales for long and short T_2 tissues. Consequently, the long T_2 tissues, which are clearly observable in the third column, seem to be saturated at the finer display scales in the fourth column. Two ROIs (5 x 5) in bone marrow and muscle are marked by red boxes in the anatomic image. The mean T_1 / T_2 for bone marrow and muscle are 364/141 ms and 1038/27 ms, respectively. Short T_2 tissues including the tibia (labeled by *a*), fibula (*b*), Achilles tendon (*c*), and peroneus longus tendon (*d*) are observed in the fourth column under different display ranges. The average T_2 in a 3 x 3 ROI in Fig. 7 is 1.0 ms for cortical bone and 15 ms for Achilles tendon. High off-resonance artifacts are detected in bone marrow and skin due to the

chemical shift between fat and water.

Fig. 8 shows the simulation results for the brain for the longitudinal magnetization time evolution using T_1 and T_2 relaxometries reconstructed from UTE-MRF. As shown in the figure, since tissue relaxometries are quantified through dictionary matching, one can look up the dictionary and generate transverse / longitudinal magnetization changes at any MRF time point.

Fig. 9 shows brain bone enhanced images and parametric maps from 3 healthy volunteers using UTE-MRF. Although UTE-MRF loses its sensitivity to ultrashort T_2 quantification when TE is fixed at 50 μs , it gains SNR and achieves higher resolution. The bone enhanced images show enhanced skulls, which were generated by dividing the M_z map reconstructed from MRF frame No. 130 (Fig. 8) by the T_1 map. Some dark spots are detected in both the T_1 and T_2 maps, especially at the lateral ventricle. Those spots (as indicated by the blue arrows) show high intensity in the bone enhanced images in S3. The results from three orthogonal planes are shown in Supporting Information Figure S2.

Bone enhanced images from the patient with facial neuromas are compared with CT images in Fig. 10. Streaking artifacts are observed in the T_2 maps, especially at the middle of the brain. The zygomatic bone and hyperintensity areas in the bone enhanced images are in good agreement with the CT images, as indicated by the red arrows.

Discussion

In this work, a UTE-MRF method was proposed to simultaneously quantify long and short / ultrashort T_2 tissues and to synthesize bone enhanced images. The sinusoidal TE pattern was incorporated with a minimal TE of 50 μs . Variable TE-induced phase changes were compensated using the B_0 map demodulated from the phases of the MRF

frames. T_1 , T_2 , and PD maps were reconstructed through dictionary matching. The longitudinal magnetization map, which was obtained by looking up the dictionary based on the quantified relaxometries, was employed to produce bone enhanced images. Simulation, phantom measurements, and in vivo studies showed the capability of UTE-MRF for detecting and quantifying musculoskeletal system mimic phantoms, tendon, cortical bone, and muscle. In vivo brain scans also demonstrated its capability for brain quantifications and producing bone enhanced images.

With the sinusoidal TE variation, the B_0 map can be directly estimated from the phase of MRF frames through the amplitude demodulation method without an additional dictionary and matching burden. TE variation causes a synchronized sinusoidal phase change as the product of TE and B_0 offset caused by chemical shift and field inhomogeneity. Calculating the field changes directly using [6] suffers from strong undersampling aliasing, resulting in poor field estimation. Here, a noniterative sliding window method (39) was used to reduce undersampling artifacts. Cao et al. chose the number of fully sampled spiral interleaves as the window length. For imaging FOV = $140 \times 140 \text{ mm}^2$ and resolution = $1.0 \times 1.0 \text{ mm}^2$, a fully sampled radial would require 220 spokes. However, a window length of 220 would tremendously decrease the tissue specificity, as it is approximately twice the TE and FA variation period (120). To balance tissue specificity and undersampling aliasing, a window size of 20 was used in this study, and the maximum TE variation within the sliding window was $(TE_{\max} - TE_{\min})/2$. Since multiple repetitions were performed to increase SNR for bone, tendon, and the rubber phantom, the actual image undersampling factor within the sliding window was 2.2. There is a tradeoff between B_0 sensitivity and image SNR in choosing TE sampling ranges. More accurate field estimation would be achieved through strong phase changes via increased TE variation. However, there is more loss of image SNR as a penalty due to the T_2/T_2^* decay effect. To avoid the impact of IR-induced phase changes along MRF frames, the last 2 periods of MRF frames were applied to estimate B_0 . Two periods (1440 ms, $2 \times 120 \times TR$) are adequate for the tissue with the longest T_1 to pass through its IR null point, e.g., for a T_1 of 2000 ms, the IR

null point is 1386 ms ($\ln(2) \times T_1$).

To achieve ultrashort TE, half-pulse excitation (duration of 0.7 ms) and radial acquisition (window length of 0.79 ms) were employed. Although T_2^* decay during excitation has an impact on the excitation profile, Pauly has shown that there is a small loss of signal and slight broadening of the slice profile for tissue with T_2 of 0.25 ms and a half pulse with a duration of 1 ms (28). Since the responses of the inversion and excitation are influenced by the relaxation times, especially T_2 (51,52), Bloch equation with relaxation times would be more accurate to model the inversion and excitation imperfections, and these effects could be modeled into dictionary using Bloch equation simulation to further improve the quantification accuracy. Excitation performance would also be degraded by hardware imperfections. To minimize timing error between RF and gradient, the RF pulse was adjusted to perform a -10 to 10 μs (in steps of 1 μs) time shift relative to the gradient. The optimal shift time of -3 μs was chosen based on the performance of the slice profile. To decrease the impact of eddy currents, a bipolar slice selection gradient was employed based on the fact that the long-term eddy currents from ramp-up and ramp-down gradients are cancelled due to their opposite polarities (31). However, residual short-term eddy currents may still distort the slice selection gradient. Better slice selection performance could be achieved by measuring the trajectory of the slice selection gradient (11). To reduce the blurriness of the T_2^* of bone ($T_2 \leq 1$ ms), a readout window of 0.79 ms was employed under an optimal window size of $0.81T_2$ (24). Off-resonance blurring was decreased by using a high readout bandwidth of 1780 Hz/pixel.

The simulation results in Fig. 4 indicate that UTE-MRF is capable of simultaneously quantifying long and short T_2 tissue components. T_1 and T_2 quantification errors in muscle almost remain constant with increased TE samplings, which suggests TE variations have little impact on long T_2 tissue. Since doubling sequence repetitions reduces T_1 / T_2 RMSEs by approximately twofold (Fig. 4a), a radial undersampling artifact is probably the primary source for the steady quantification errors. Since TE varies from frame to frame, it introduces T_2^* weighting in the MRF image series.

According to the results in supplementary Table 1, the T_2^* effect has little impact on long T_2 muscle because the maximum TE variation of 0.6 ms is much smaller than the nominal T_2 (32 ms) and T_2^* (25 ms) values of muscle. The impact of the T_2^* effect increases for shorter nominal T_2 and T_2^* values. For the bone total water with the shortest T_2 and T_2^* , the measured T_2 from UTE-MRF is close to its nominal T_2^* value. Although cortical bone free water has longer T_2 values than bone total water and tendon, its quantification accuracy is the poorest due to its low proton density. At low image SNR under 3 UTE-MRF reps, an increment of the TE sampling range could enhance the MRF specificities for ultrashort T_2 tissues and improve ultrashort T_2 tissue quantification. As suggested by the simulation performance, an optimal TE_{max} of 0.6 ms was used for the phantom and in vivo experiments, and the TE_{min} of 0.05 ms was unchanged throughout the experiments.

For the phantom quantifications in Fig. 6, most of the relaxometries in UTE-MRF were in good agreement with the gold standards, except for the T_2 of the No.4 rubber plug and the oil tube. In UTE-MRF, the chemical shift-caused frequency offset is encoded into the phase of the MRF frames, then estimated using [6] and compensated in the MRF frames before dictionary matching. The oil spectrum shows 6 peaks (Supporting Information Figure S1), which is similar to the Fig. 8 in the work of Reeder et al (49). Mono-exponential fitting in SE method underestimates the T_2 of the oil sample which actually contains multi-components. While multicomponent analysis may be needed for quantifying T_2 , the multicomponent effect has minimal impact on UTE-MRF since the maximum TE used in UTE-MRF was 0.6 ms.

The average T_2 of cortical bone and tendon from the chosen ROI was 1.0 ms and 15.0 ms, respectively. Bicomponent analyses have shown that cortical bone possesses bound water (T_2^* of 0.36 ms) and free water (T_2^* of 5.56 ms) (53). Tendon shows similar bicomponent characteristics, with a shorter T_2^* of 0.88 ms and a longer T_2^* of 25.58 ms (54). The TE variations from 0.05 ms to 0.6 ms enable UTE-MRF to detect signals from both bound and free water in cortical bone and tendon, as demonstrated in the

simulation results (Fig. 4b). Therefore, the T_1 and T_2 quantified from UTE-MRF are the apparent T_1 and T_2 from both short T_2 and long T_2 water components of bone and tendon.

The in vivo brain relaxometry quantification and bone enhanced images are achieved using UTE-MRF (Fig. 9 and Fig. 10). Although the sensitivity of MRF to T_2 was decreased by the halved FA trains in the patient study, the bone structures from UTE-MRF were still mostly consistent with the CT images. The dark spots in the in vivo T_1 and T_2 maps only appeared at areas filled with cerebrospinal fluid. Those dark spots were likely caused by inconsistent excitation due to flow effect, since two half pulses may excite different moving spins. Consequently, the mismatched flow spins may lead to signal error. To obtain high-quality bone enhanced images, TE was minimized to $50 \mu\text{s}$ in brain scans. However, the T_2 sensitivity of UTE-MRF for short T_2 tissues was reduced as a penalty. For voxels with mixed short T_2 and long T_2 components, UTE-MRF measures an apparent T_1 and T_2 from the overall signal. To resolve the MRF signal into long and short T_2 components, a multicomponent analysis method could be employed and modeled into dictionary (3).

The proposed UTE-MRF method was validated via simulations, phantoms, and in vivo experiments. However, there are some limitations of the current 2D UTE-MRF approach. First, this approach does not totally encompass imaging imperfections such as B_1 inhomogeneity and a nonideal slice profile, which limits the quantification performance. To correct B_1 inhomogeneity, B_1 maps can be acquired either independently (42) or in association with MRF data (55). To avoid slice profile imperfections, spiral acquisition-based 3D MRF has been demonstrated (41,42). Furthermore, the increase in SNR due to 3D volume excitation could also benefit the characterization of low spin density tissues such as bone. The current method still requires an acquisition time of ~ 1 min for a single slice, and thus the scan efficiency of UTE-MRF limits its clinical applications. The excitation time would be halved with hard pulse volume excitation in 3D (56,57). To further speed up the acquisition, effective 3D k-space sampling could be used (58). As part of the future implementation

of UTE-MRF techniques, we will adapt the above and other methods to accelerate the process. Second, although the T_2 of cortical bone from the chosen ROI is in agreement with previous work (17), the cortical bone quantification in Fig. 7 suffers from the strong streaking artifact from bone marrow. This issue could be addressed by either separating water and fat before dictionary matching (25,37) or characterizing fat in the MRF dictionary (34). Additionally, the experiment could be optimized by optimizing UTE-MRF FA and TE variation patterns (59). Third, ultrashort T_2 components from the myelin membrane or membrane structures in white matter and gray matter are explored by previous UTE methods (60,61). With a TE of 0.05 ms, UTE-MRF acquires those ultrashort T_2 components; however, this phenomenon was not fully studied in this work. Fourth, to accomplish attenuation correction in PET/MR, the bone enhanced images must have a quantitative CT unit by assigning the CT values to different tissues segmented from MR (19,62) or a machine learning-based method (63).

Conclusion

An ultrashort echo time MR fingerprinting (UTE-MRF) method with sinusoidal echo time variations was proposed and tested via simulations, phantom, and in vivo experiments. The capability of the method to quantify tendon and cortical bone could benefit studies of age-related bone degradation and other musculoskeletal abnormalities. Furthermore, UTE-MRF could be used in PET/MRI systems to simultaneously quantify brain tissues and aid PET attenuation correction with simultaneously synthesized bone enhanced images.

Acknowledgments

The authors would like to acknowledge Dr. Kang Wang and Dr. Jin Jin from the First Affiliated Hospital of Zhejiang University for the help and discussions on the patient scans.

References

1. Du J, Bydder GM. Qualitative and quantitative ultrashort-TE MRI of cortical bone. *NMR Biomed.* 2013;26(5):489-506.
2. Chang EY, Du J, Chung CB. UTE Imaging in the Musculoskeletal System. *J. Magn. Reson. Imaging.* 2015;41(4):870-883.
3. Boucneau T, Cao P, Tang SY, Han MS, Xu D, Henry RG, Larson PEZ. In vivo characterization of brain ultrashort-T₂ components. *Magn. Reson. Med* 2018;80(2):726-735.
4. Wiesinger F, Sacolick LI, Menini A, Kaushik SS, Ahn S, Veit-Haibach P, Delso G, Shanbhag DD. Zero TE MR Bone Imaging in the Head. *Magn Reson Med.* 2016;75(1):107-114.
5. Larson PEZ, Han MS, Krug R, Jakary A, Nelson SJ, Vigneron DB, Henry RG, McKinnon G, Kelley DAC. Ultrashort echo time and zero echo time MRI at 7T. *Magn. Reson. Mater. Phy.* 2016;29(3):359-370.
6. Johnson EM, Vyas U, Ghanouni P, Pauly KB, Pauly JM. Improved cortical bone specificity in UTE MR Imaging. *Magn Reson Med.* 2017;77(2):684-695.
7. Emid S, Creyghton JHN. High-Resolution Nmr Imaging in Solids. *Physica B & C* 1985;128(1):81-83.
8. Balcom BJ, MacGregor RP, Beyea SD, Green DP, Armstrong RL, Bremner TW. Single-point ramped imaging with T₁ enhancement (SPRITE). *J. Magn. Reson. Ser. A* 1996;123(1):131-134.
9. Fernandez-Seara MA, Wehrli SL, Wehrli FW. Multipoint mapping for imaging of semi-solid materials. *J. Magn. Reson.* 2003;160(2):144-150.
10. Grodzki DM, Jakob PM, Heismann B. Ultrashort echo time imaging using pointwise encoding time reduction with radial acquisition (PETRA). *Magn Reson Med.* 2012;67(2):510-518.
11. Manhard MK, Harkins KD, Gochberg DF, Nyman JS, Does MD. 30-Second Bound and Pore Water Concentration Mapping of Cortical Bone Using 2D UTE With

- Optimized Half-Pulses. *Magn Reson Med.* 2017;77(3):945-950.
12. Ma YJ, Lu X, Carl M, Zhu YC, Szeverenyi NM, Bydder GM, Chang EY, Du J. Accurate T-1 mapping of short T-2 tissues using a three-dimensional ultrashort echo time cones actual flip angle imaging-variable repetition time (3D UTE-Cones AFI-VTR) method. *Magn Reson Med.* 2018;80(2):598-608.
 13. Li XJ, Majumdar S. Quantitative MRI of Articular Cartilage and Its Clinical Applications. *J. Magn. Reson. Imaging* 2013;38(5):991-1008.
 14. Williams A, Qian Y, Golla S, Chu CR. UTE-T2* mapping detects sub-clinical meniscus injury after anterior cruciate ligament tear. *Osteoarthr Cartilage* 2012;20(6):486-494.
 15. Abbasi-Rad S, Rad HS. Quantification of Human Cortical Bone Bound and Free Water in Vivo with Ultrashort Echo Time MR Imaging: A Model-based Approach. *Radiology* 2017;283(3):861-871.
 16. Larson PEZ, Gurney PT, Nayak K, Gold GE, Pauly JM, Nishimura DG. Designing long-T-2 suppression pulses for ultrashort echo time imaging. *Magn Reson Med.* 2006;56(1):94-103.
 17. Du J, Takahashi AM, Bae WC, Chung CB, Bydder GM. Dual Inversion Recovery, Ultrashort Echo Time (DIR UTE) Imaging: Creating High Contrast for Short-T-2 Species. *Magn Reson Med.* 2010;63(2):447-455.
 18. Ma LH, Meng QF, Chen YM, Zhang ZH, Sun HX, Deng DM. Preliminary use of a double-echo pulse sequence with 3D ultrashort echo time in the MRI of bones and joints. *Exp. Ther. Med.* 2013;5(5):1471-1475.
 19. Wiesinger F, Bylund M, Yang J, Kaushik S, Shanbhag D, Ahn S, Jonsson JH, Lundman JA, Hope T, Nyholm T, Larson P, Cozzini C. Zero TE-based pseudo-CT image conversion in the head and its application in PET/MR attenuation correction and MR-guided radiation therapy planning. *Magn Reson Med.* 2018;80(4):1440-1451.
 20. Ma D, Gulani V, Seiberlich N, Liu KC, Sunshine JL, Duerk JL, Griswold MA. Magnetic resonance fingerprinting. *Nature* 2013;495(7440):187-192.
 21. Mehta BB, Coppo S, McGivney DF, Hamilton JI, Chen Y, Jiang Y, Ma D, Seiberlich

- N, Gulani V, Griswold MA. Magnetic resonance fingerprinting: a technical review. *Magn Reson Med.* 2019;81(1):25-46.
22. Chen Y, Jiang Y, Pahwa S, Ma D, Lu L, Twieg MD, Wright KL, Seiberlich N, Griswold MA, Gulani V. MR Fingerprinting for Rapid Quantitative Abdominal Imaging. *Radiology* 2016;279(1):278-286.
23. Liao CY, Wang K, Cao XZ, Li YP, Wu DC, Ye HH, Ding QP, He HJ, Zhong JH. Detection of Lesions in Mesial Temporal Lobe Epilepsy by Using MR Fingerprinting. *Radiology* 2018;288(3):804-812.
24. Rahmer J, Bornert P, Groen J, Bos C. Three-dimensional radial ultrashort echo-time imaging with T(2) adapted sampling. *Magn. Reson. Med.* 2006;55(5):1075-1082.
25. Cloos MA, Knoll F, Zhao TJ, Block KT, Bruno M, Wiggins GC, Sodickson DK. Multiparametric imaging with heterogeneous radiofrequency fields. *Nat Commun* 2016;7: 12445.
26. Jiang Y, Ma D, Seiberlich N, Gulani V, Griswold MA. MR Fingerprinting Using Fast Imaging with Steady State Precession (FISP) with Spiral Readout. *Magn Reson Med.* 2015;74(6):1621-1631.
27. Nielsen HTC, Gold GE, Olcott EW, Pauly JM, Nishimura DG. Ultra-short echo-time 2D time-of-flight MR angiography using a half-pulse excitation. *Magn Reson Med* 1999;41(3):591-599.
28. Pauly JM. Selective Excitation for Ultrashort Echo Time Imaging. *Encycl Magn Reson* 2012;1:381-388.
29. Winkelmann S, Schaeffter T, Koehler T, Eggers H, Doessel O. An optimal radial profile order based on the golden ratio for time-resolved MRI. *IEEE Trans Med Imaging* 2007;26(1):68-76.
30. Hargreaves BA, Cunningham CH, Nishimura DG, Conolly SM. Variable-rate selective excitation for rapid MRI sequences. *Magn Reson Med.* 2004;52(3):590-597.
31. Du J, Hamilton G, Takahashi A, Bydder M, Chung CB. Ultrashort echo time spectroscopic imaging (UTESI) of cortical bone. *Magn Reson Med.* 2007;58(5):1001-1009.

32. Wundrak S, Paul J, Ulrici J, Hell E, Rasche V. A Small Surrogate for the Golden Angle in Time-Resolved Radial MRI Based on Generalized Fibonacci Sequences. *IEEE Trans. Med. Imaging* 2015;34(6):1262-1269.
33. Rieger B, Zimmer F, Zapp J, Weingartner S, Schad LR. Magnetic Resonance Fingerprinting Using Echo-Planar Imaging: Joint Quantification of T-1 and T-2* Relaxation Times. *Magn Reson Med.* 2017;78(5):1724-1733.
34. Cencini M, Biagi L, Kaggie JD, Schulte RF, Tosetti M, Buonincontri G. Musculoskeletal MR Fingerprinting with dictionary-based fat and water separation. In Proceedings of the 26th Annual Meeting of ISMRM, Paris, 2018. Abstract1025.
35. Hennig J, Weigel M, Scheffler K. Calculation of flip angles for echo trains with predefined amplitudes with the extended phase graph (EPG)-algorithm: Principles and applications to hyperecho and TRAPS sequences. *Magn Reson Med.* 2004;51(1):68-80.
36. Weigel M. Extended Phase Graphs: Dephasing, RF Pulses, and Echoes - Pure and Simple. *J. Magn. Reson. Imaging* 2015;41(2):266-295.
37. Koolstra K, Webb A, Koken P, Nehrke K, Bornert P. Water-Fat Separation in Spiral Magnetic Resonance Fingerprinting using Conjugate Phase Reconstruction. In Proceedings of the 26th Annual Meeting of ISMRM, Paris, 2018. Abstract 681.
38. Rappaport TS. *Wireless communications : principles and practice.* Upper Saddle River, N.J.: Prentice Hall PTR; 1996.
39. Cao XZ, Liao CY, Wang ZX, Chen Y, Ye HH, He HJ, Zhong JH. Robust sliding-window reconstruction for Accelerating the acquisition of MR fingerprinting. *Magn Reson Med.* 2017;78(4):1579-1588.
40. Li Q, Cao XZ, Ye HH, Liao CY, He HJ, Zhong JH. Quantification of long and ultra-short relaxation times in tissues with ultra-short TE MR fingerprinting. In Proceedings of the 26th Annual Meeting of ISMRM, Paris, 2018. Abstract 680.
41. Liao CY, Bilgic B, Manhard MK, Zhao B, Cao XZ, Zhong JH, Wald LL, Setsompop K. 3D MR fingerprinting with accelerated stack-of-spirals and hybrid sliding-window and GRAPPA reconstruction. *Neuroimage* 2017;162:13-22.
42. Ma D, Jiang Y, Chen Y, McGivney D, Mehta B, Gulani V, Griswold M. Fast 3D

- magnetic resonance fingerprinting for a whole-brain coverage. *Magn Reson Med* 2018;79(4):2190-2197.
43. Fessler JA, Sutton BP. Nonuniform fast Fourier transforms using min-max interpolation. *IEEE Trans Signal Process* 2003;51(2):560-574.
 44. Walsh DO, Gmitro AF, Marcellin MW. Adaptive reconstruction of phased array MR imagery. *Magn Reson Med*. 2000;43(5):682-690.
 45. Deshmane A, McGivney D, Badve C, Gulani V, Griswold M. Dictionary approach to partial volume estimation with MR fingerprinting: validation and application to brain tumor segmentation. In *Proceedings of the 25th Annual Meeting of ISMRM, Honolulu, 2017*. Abstract 132.
 46. Gold GE, Han E, Stainsby J, Wright G, Brittain J, Beaulieu C. Musculoskeletal MRI at 3.0 T: relaxation times and image contrast. *Am. J. Roentgenol* 2004;183(2):343-351.
 47. Manhard MK, Horch RA, Gochberg DF, Nyman JS, Does MD. In Vivo Quantitative MR Imaging of Bound and Pore Water in Cortical Bone. *Radiology* 2015;277(3):927-927.
 48. Zwart NR, Johnson KO, Pipe JG. Efficient sample density estimation by combining gridding and an optimized kernel. *Magn Reson Med*. 2012;67(3):701-710.
 49. Reeder SB, Sirlin CB. Quantification of Liver Fat with Magnetic Resonance Imaging. *Magn Reson Imaging Clinics* 2010;18(3):337-357.
 50. Barral JK, Gudmundson E, Stikov N, Etezadi-Amoli M, Stoica P, Nishimura DG. A Robust Methodology for In Vivo T-1 Mapping. *Magn Reson Med*. 2010;64(4):1057-1067.
 51. Carl M, Bydder M, Du JA, Takahashi A, Han E. Optimization of RF Excitation to Maximize Signal and T(2) Contrast of Tissues With Rapid Transverse Relaxation. *Magn Reson Med*. 2010;64(2):481-490.
 52. Kellman P, Herzka DA, Hansen MS. Adiabatic Inversion Pulses for Myocardial T1 Mapping. *Magn Reson Med*. 2014;71(4):1428-1434.
 53. Chen J, Carl M, Ma YJ, Shao HD, Lu X, Chen BM, Chang EY, Wu ZH, Du J. Fast volumetric imaging of bound and pore water in cortical bone using three-

- dimensional ultrashort-TE (UTE) and inversion recovery UTE sequences. *NMR in Biomed.* 2016;29(10):1373-1380.
54. Juras V, Apprich S, Szomolanyi P, Bieri O, Deligianni X, Trattnig S. Bi-exponential T2* analysis of healthy and diseased Achilles tendons: an in vivo preliminary magnetic resonance study and correlation with clinical score. *Eur. Radiol.* 2013;23(10):2814-2822.
55. Ma D, Coppo S, Chen Y, McGivney DF, Jiang Y, Pahwa S, Gulani V, Griswold MA. Slice Profile and B-1 Corrections in 2D Magnetic Resonance Fingerprinting. *Magn Reson. Med.* 2017;78(5):1781-1789.
56. Diwoky C, Liebmann D, Neumayer B, Reinisch A, Knoll F, Strunk D, Stollberger R. Positive contrast of SPIO-labeled cells by off-resonant reconstruction of 3D radial half-echo bSSFP. *NMR Biomed.* 2015;28(1):79-88.
57. Wiesinger F, Janich M, Ljungberg E, Barker G, Solana AB. Silent, 3D MR Parameter Mapping using Magnetization Prepared Zero TE. In Proceedings of the 26th Annual Meeting of ISMRM, Paris, 2018. Abstract 61.
58. Zhang J, Feng L, Otazo R, Kim SG. Rapid dynamic contrast-enhanced MRI for small animals at 7T using 3D ultra-short echo time and golden-angle radial sparse parallel MRI. *Magn Reson Med.* 2019;81(1):140-152.
59. Zhao B, Haldar JP, Setsompop K, Wald LL. Optimal Experiment Design for Magnetic Resonance Fingerprinting. *IEEE Eng Med Bio.* 2016:453-456.
60. Horch RA, Gore JC, Does MD. Origins of the Ultrashort-T-2 H-1 NMR Signals in Myelinated Nerve: A Direct Measure of Myelin Content? *Magn Reson Med.* 2011;66(1):24-31.
61. Fan SJ, Ma YJ, Chang EY, Bydder GM, Du J. Inversion recovery ultrashort echo time imaging of ultrashort T-2 tissue components in ovine brain at 3 T: a sequential D2O exchange study. *NMR Biomed.* 2017;30(10).
62. Juttukonda MR, Mersereau BG, Chen Y, Su Y, Rubin BG, Benzinger TLS, Lalush DS, An H. MR-based attenuation correction for PET/MRI neurological studies with continuous-valued attenuation coefficients for bone through a conversion from R2* to CT-Hounsfield units. *Neuroimage* 2015;112:160-168.

63. Liu F, Jang H, Kijowski R, Bradshaw T, McMillan AB. Deep Learning MR Imaging-based Attenuation Correction for PET/MR Imaging. *Radiology* 2018;286(2):676-684.
64. Badve C, Dastmalchian S, Kilinc O, McGivney D, Ma D, Griswold M, Sunshine J, Gulani V, Barnholtz-Sloan J, Sloan A. Texture Analysis of Mr Fingerprinting in Adult Brain Tumors. *Neuro-Oncology* 2017;19:162-162.
65. Anderson CE, Wang CY, Gu YN, Darrach R, Griswold MA, Yu X, Flask CA. Regularly incremented phase encoding - MR fingerprinting (RIPE-MRF) for enhanced motion artifact suppression in preclinical cartesian MR fingerprinting. *Magn Reson Med.* 2018;79(4):2176-2182.

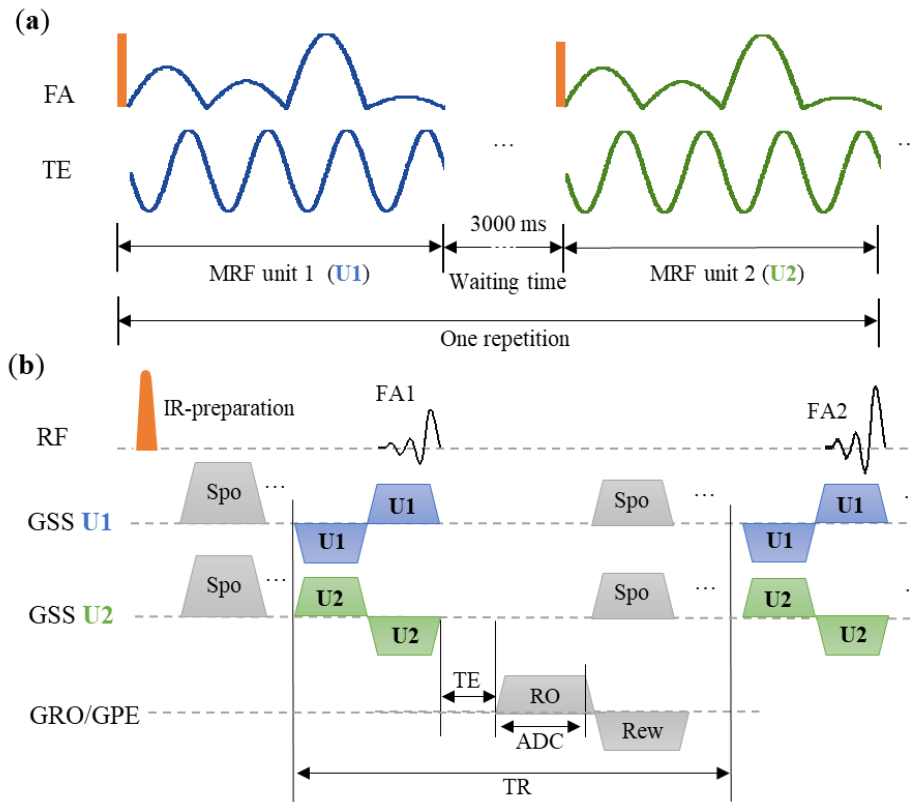


Fig. 1. Sequence diagram of UTE-MRF. UTE-MRF is acquired with the IR-FISP sequence utilizing half-pulse excitation and radial acquisition. The fingerprint-like scan shown in (a) is called an MRF unit, where the flip angle and echo time varies from TR to TR. A fixed repetition time of 6 ms was used to increase scan efficiency. One UTE-MRF repetition comprises two MRF units. Details of the RF and gradient timing in a single TR are shown in (b). The slice selection gradient polarization is fixed within one MRF unit (U1, in blue) but is inverted for the next MRF unit (U2, in green). The k-space trajectories of the same MRF frame are uniformly distributed over a unit circle when multiple repetitions are performed. Spo, RO, Rew indicate the gradients of spoiler, readout, andrewinder.

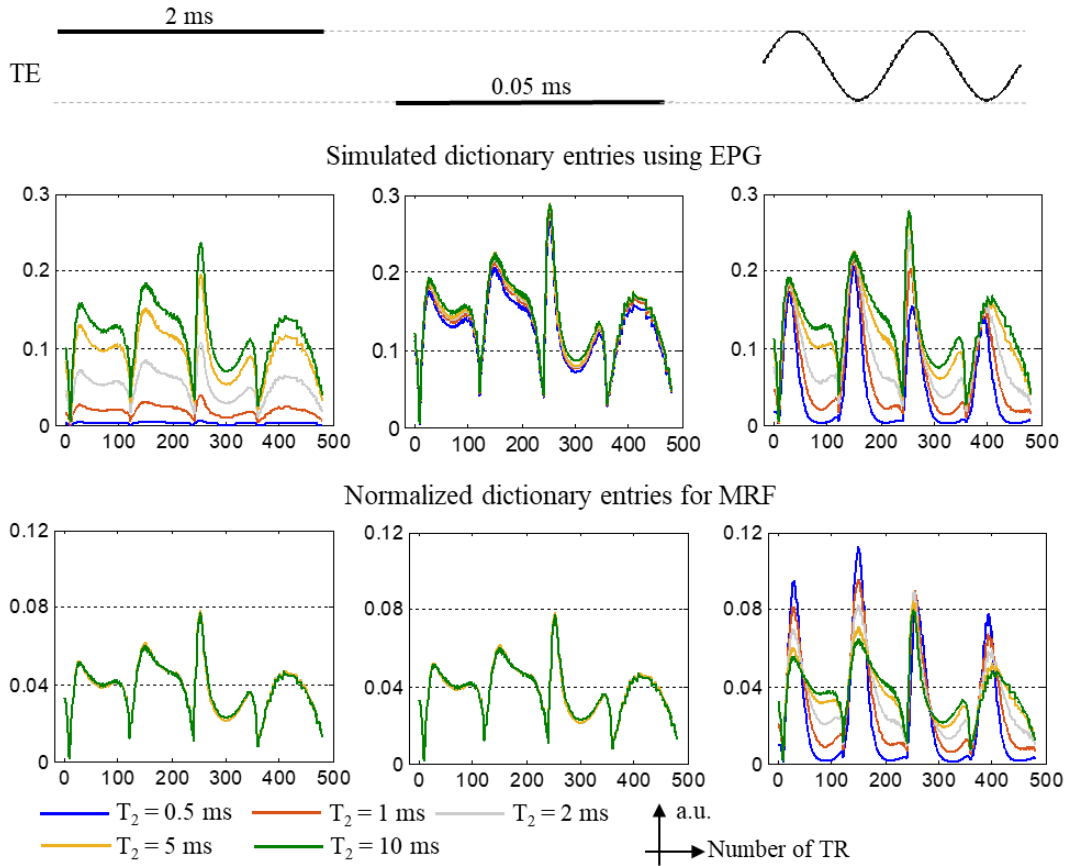
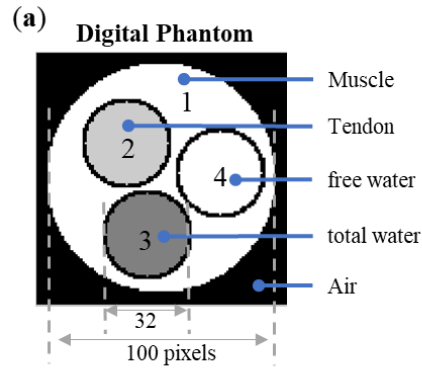


Fig. 2. Simulations of the impact of TE patterns on MRF signal evolutions (fingerprints) under the same T_1 of 180 ms and increased T_2 of 0.5, 1, 2, 5, and 10 ms. Two single TEs of 2 and 0.05 ms were used in the first and second columns, respectively. In the last column, TE was varied in a sinusoidal pattern from 0.05 to 2 ms. For dictionary entries at constant TEs (the first two columns), the difference among simulated fingerprints (second row) disappeared after dictionary normalization (last row). However, these fingerprints under sinusoidal TE could be differentiated both before and after dictionary normalization (last column).



(b) Tissue Parameters

	T_1 (ms)	T_2 (ms)	T_2' (ms)	PD	SNR
Muscle	1400	32	114	1	28
Tendon	621	3	9.9	0.8	20
Total water	246	1.2	1.7	0.7	14
Free water	524	3.5	7.6	0.3	7

Fig. 3. Digital phantom and its corresponding simulation parameters. The peripheral cylinder has a diameter of 100 (pixels), and the inserted small cylinders have a diameter of 32 (pixels). Tissue parameters are chosen based on the literature (16,46,47). T_2^* values are 25 ms for muscle, 2.3 ms for tendon, 0.7 ms for total water, and 2.4 ms for free water

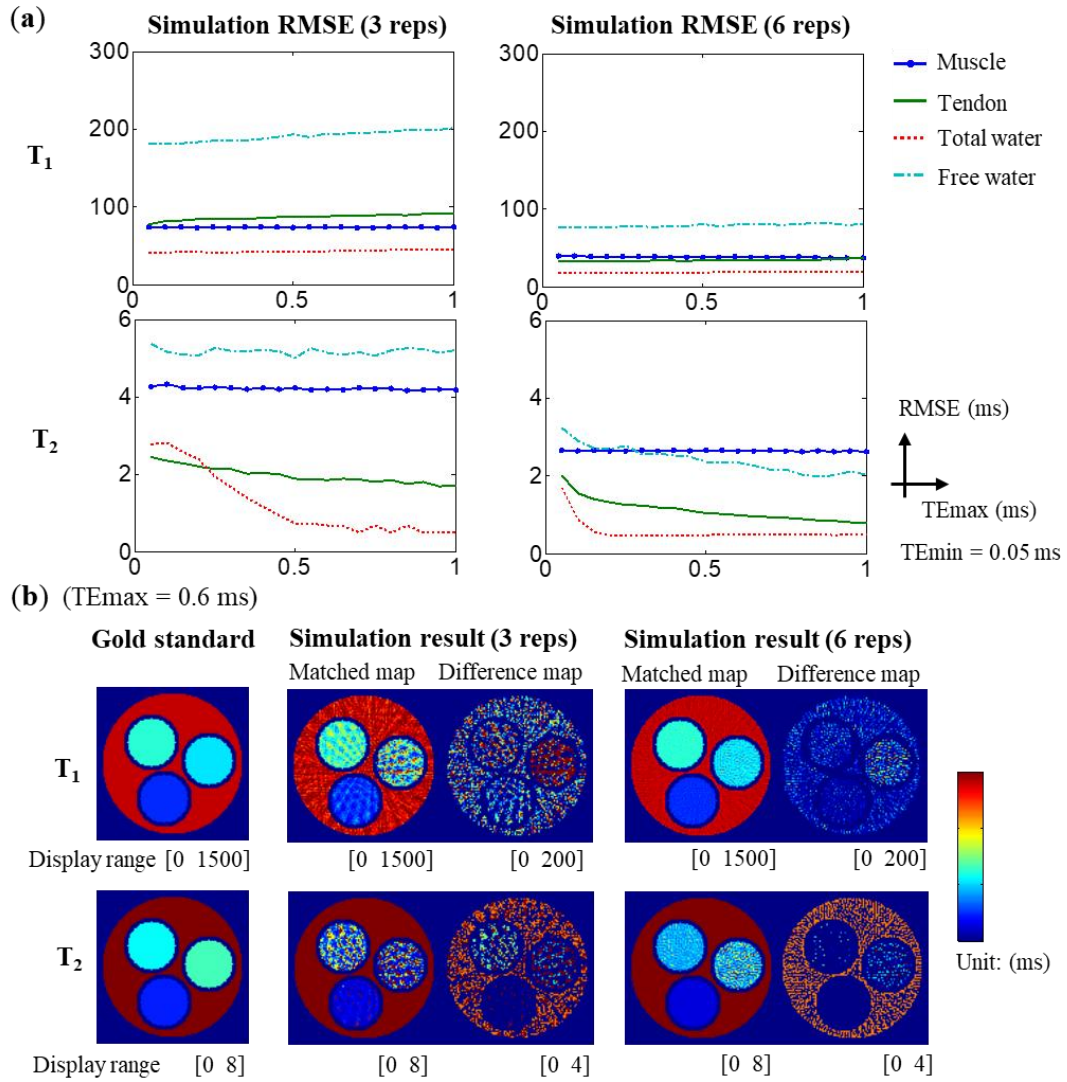


Fig. 4. Simulation results for the digital phantom with increased TE sampling ranges depending on maximum TE ($T_{E_{max}}$), where $T_{E_{min}} = 0.05$ ms and $T_{E_{max}}$ increases from 0.05 to 1 ms in steps of 0.05 ms. (a) shows the comparisons of the average quantification errors for each tissue under 3 and 6 repetitions (reps). As the TE sampling range increases, decreases in T_2 quantification errors for tendon, total water, and free water are observed. Meanwhile, the T_1 and T_2 quantification performances for long T_2 muscle are almost unchanged. (b) shows an example of reconstructed T_1 and T_2 maps under $T_{E_{max}}$ of 0.6 ms and their comparisons with gold standards. The streaking artifacts from the undersampled radial trajectory in 3 reps are largely reduced with 3 more reps.

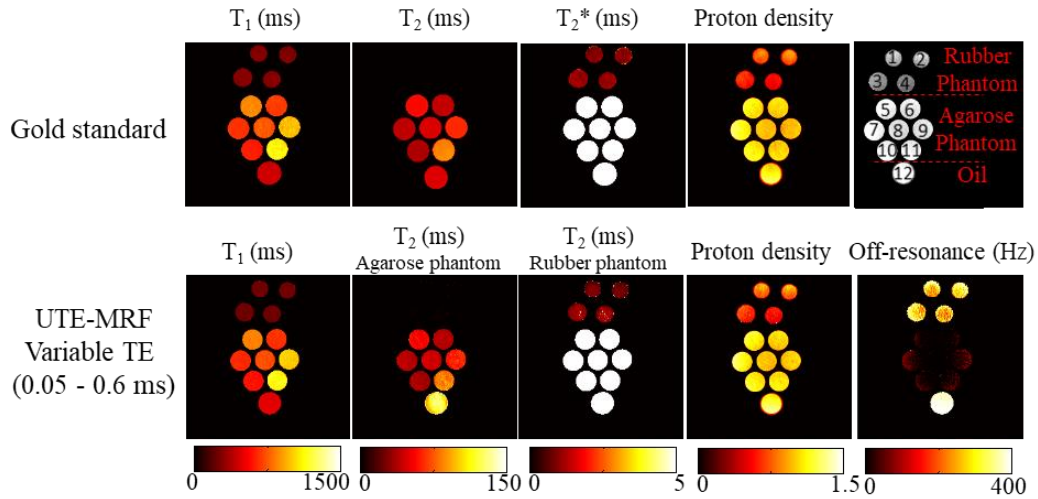
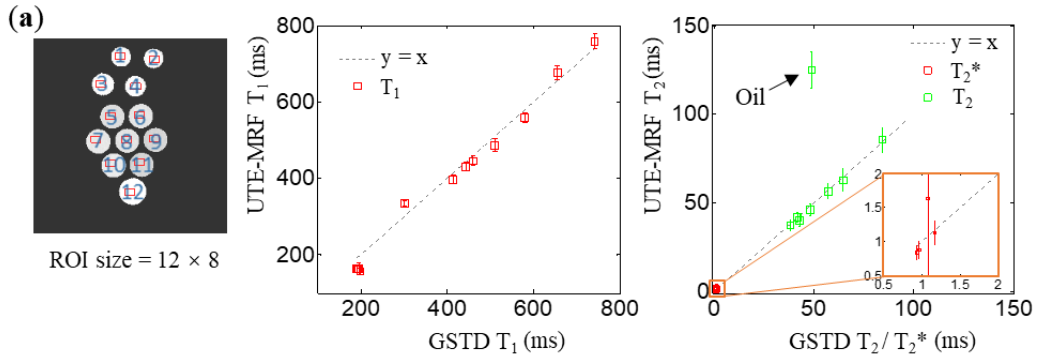


Fig. 5. Quantitative multiparametric maps in the phantom measured using the UTE-MRF ($T_{Emin} = 0.05$ ms and $T_{Emax} = 0.6$ ms) and gold standard methods. Each column shares the same color bar at the bottom. Samples of the phantom are indexed from 1 to 12 as shown at the upper right corner. Because the phantom has a large T_2 variation from approximately 1 ms to nearly 100 ms, the T_2 map from UTE-MRF is displayed at two scales: [0, 150] ms in the second column to visualize long T_2 tissues (agarose phantom and oil tube) and [0, 5] ms in the third column to visualize the short T_2 rubber phantom. Since the rubber signal is difficult to detect with the SE sequence under the minimum TE of 15 ms, the gold standard T_2^* of the rubber phantom is used as an alternative in comparison with the T_2 measured from UTE-MRF. Proton density maps are normalized by the average intensity of the oil tube.



(b) UTE-MRF Quantification Results from Chosen ROIs

(ms)	# 1	# 2	# 3	# 4	# 5	# 6
T_1	163 ± 10	164 ± 8	158 ± 9	164 ± 15	559 ± 13	446 ± 13
T_2	0.88 ± 0.14	0.84 ± 0.11	1.13 ± 0.18	1.52 ± 1.36	56 ± 5	40 ± 3
(ms)	# 7	# 8	# 9	# 10	# 11	# 12 (oil)
T_1	430 ± 11	487 ± 16	676 ± 17	397 ± 12	759 ± 19	335 ± 7
T_2	42 ± 3	45 ± 3	62 ± 2	37 ± 3	85 ± 7	122 ± 11

Fig. 6. Comparisons of T_1 and T_2 quantifications between UTE-MRF ($TE_{min} = 0.05$ ms and $TE_{max} = 0.6$ ms) and gold standard from the chosen ROIs in the phantom. (a) Plots of T_1 and T_2 from UTE-MRF versus the gold standard in twelve chosen ROIs (red boxes, size of 12×8 pixels), where the T_2 values of the rubber phantom are compared with the gold standard T_2^* (red marker) and the T_2 values of the agarose phantom are compared with gold standard T_2 (green marker). (b) T_1 and T_2 in UTE-MRF (mean \pm SD) from the chosen ROIs.

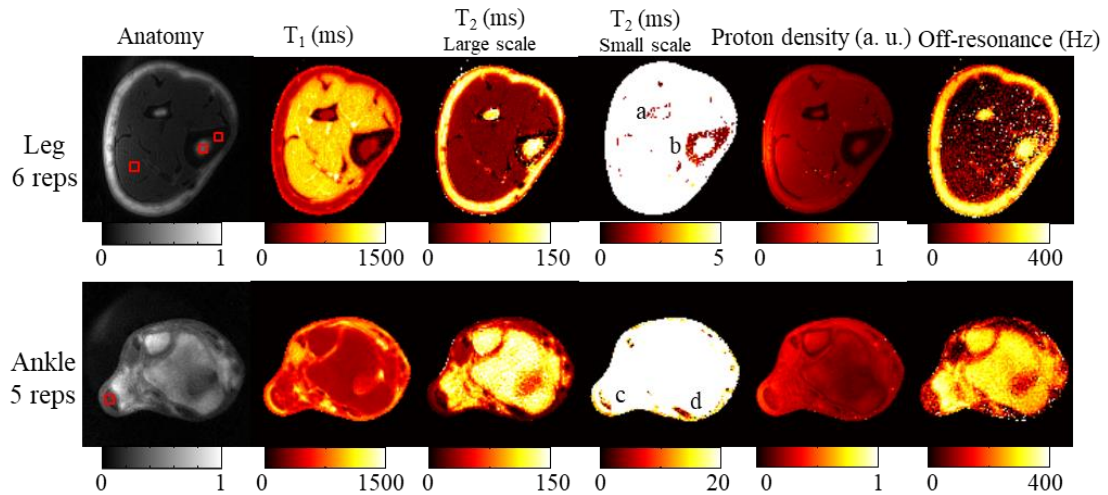


Fig. 7. In vivo results of leg and ankle (resolution = $1.0 \times 1.0 \text{ mm}^2$). The images were acquired with $TE_{\text{min}} = 0.05 \text{ ms}$, $TE_{\text{max}} = 0.6 \text{ ms}$, TE variation period = 120, and reps = 6 for leg and 5 for ankle. Tibia (a), fibula (b), Achilles tendon (c), and peroneus longus tendon (d) are detected and quantified in the fourth column. Two 5×5 ROIs are selected among muscle and bone marrow and 3×3 ROIs among fibula and Achilles tendon. The average T_2 value is 1.0 ms in the chosen fibula and 15 ms in the Achilles tendon.

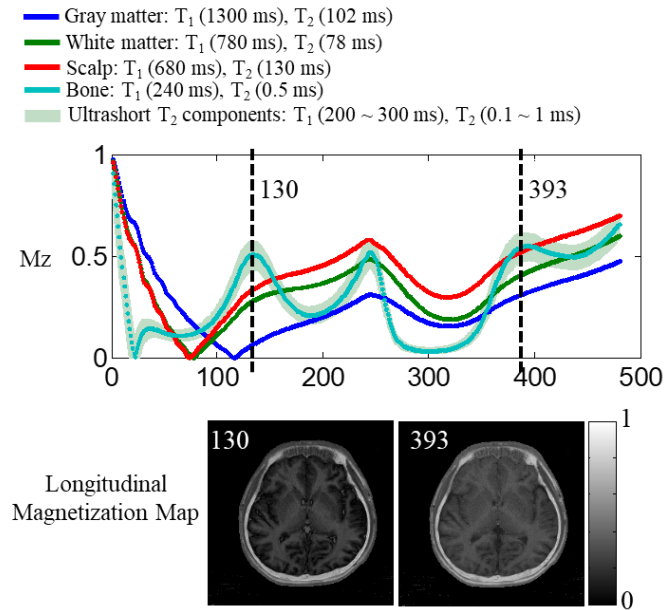


Fig. 8. Simulations of longitudinal magnetization for bone and soft tissue in the brain using EPG. Longitudinal magnetization maps at MRF No. 130 and 393 are displayed at the bottom, where bone is highlighted.

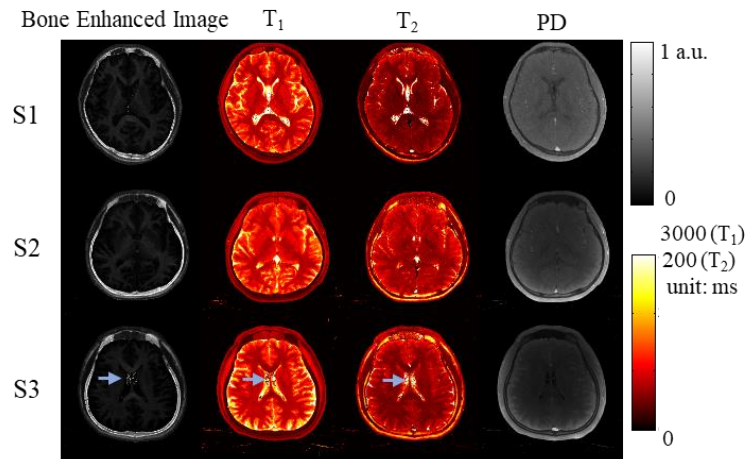


Fig. 9. Brain quantifications from 3 healthy volunteers using UTE-MRF. Volunteers are numbered from S1 to S3. Bone enhanced images and PD maps are normalized and share the same gray color bar at the upper right corner. T₁ and T₂ maps share the same color bar but with different display scales at the lower right corner.

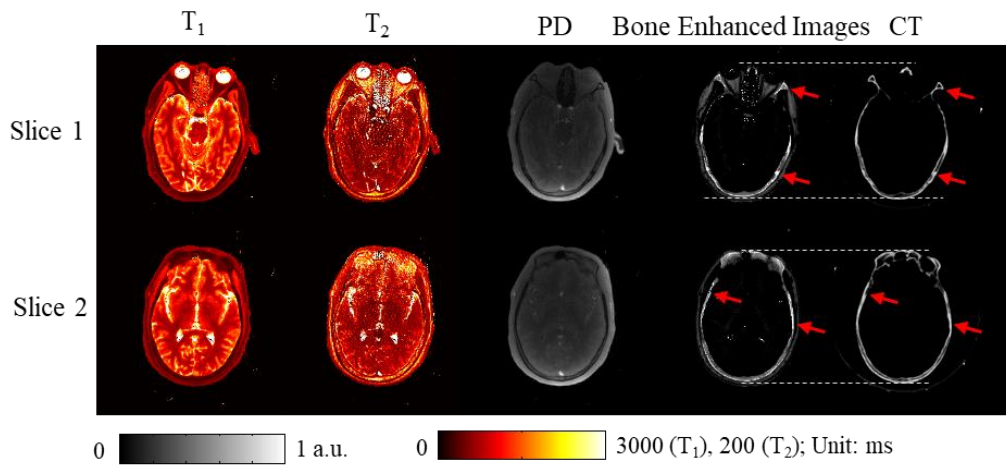


Fig. 10. Bone enhanced images, T₁, T₂, and PD maps from a tumor patient using 5 UTE-MRF reps and a constant TE of 0.05 ms (resolution = 0.75 x 0.75 mm²). Soft tissues in bone enhanced images are highly suppressed compared to the longitudinal magnetization maps in Fig. 8. The structures of skull produced by UTE-MRF are in good agreement with the CT images, especially the bone density variations indicated by the red arrows.

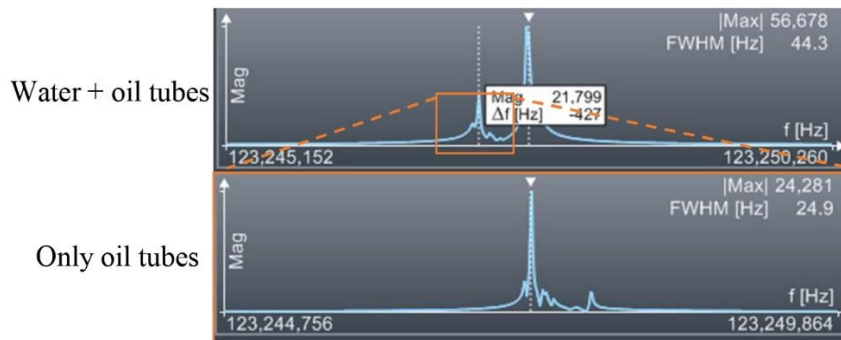
Supporting information

Supporting Information Figure S1. Spectrums of water and oil tubes. The first row (water and oil tubes) shows two major peaks, one is from water and the other is from oil. Only oil sample is scanned in the second row, where multiple peaks could be observed.

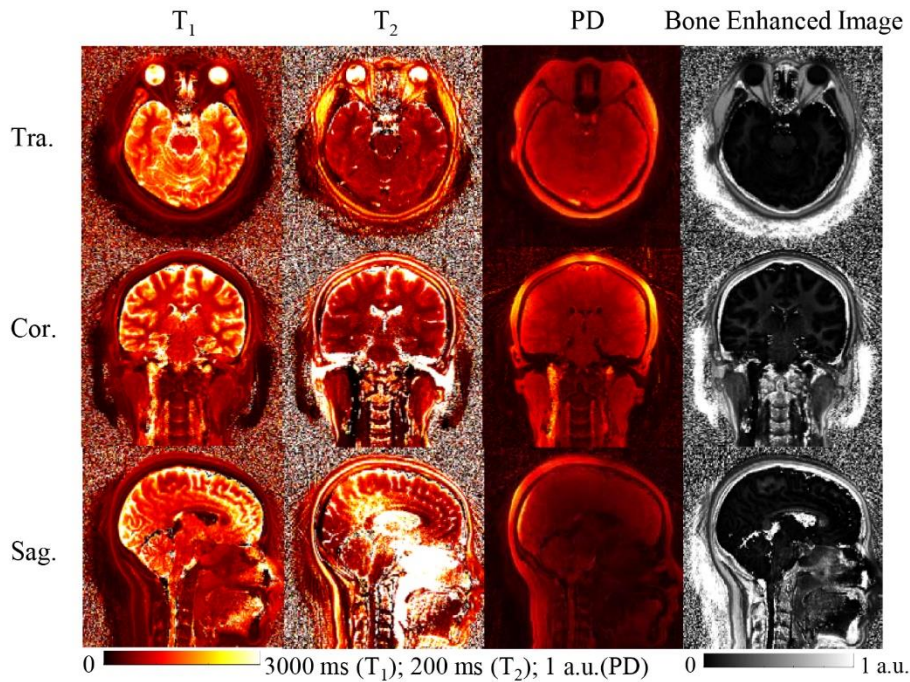
Supporting Information Figure S2. Brain quantifications from 3 orthogonal planes in one healthy volunteer using the same in vivo imaging parameters as the main text. The sponges around the ears and below the head are detected and appear dark in T_1 maps and bright in bone enhanced images. Although TE is minimized to 50 μs to maximize SNR, UTE-MRF loses its sensitivity to short and ultrashort T_2 tissues (Fig. 2). Therefore, the T_2 of sponges and bone is misestimated. There are large T_2 errors at nasal cavity, ventricle, and skull basis especially in sagittal scan. This is highly probably caused by the flow induced signal mismatching in ventricle and the absence of signal in nasal cavity and skull bases.

Supporting Information TABLE S1. The Comparisons between the Nominal Relaxation Times and the Average Measurements from UTE-MRF.

Supporting Information Video S1. The comparisons between the phase images (under 6 times of repetitions) before (left) and after (right) sliding window (window size = 20). Strong radial undersampling streaking artifact at left phase images is substantially reduced after sliding window. Therefore, radial undersampling aliasing contributes to most of the noise term at equation [6] at the main text. Thus the noise term in phase images is ignored after sliding window.



Supporting Information Figure S1. Spectrums of water and oil tubes. The first row (water and oil tubes) shows two major peaks, one is from water and the other is from oil. Only oil sample is scanned in the second row, where multiple peaks could be observed.



Supporting Information Figure S2. Brain quantifications from 3 orthogonal planes in one healthy volunteer using the same in vivo imaging parameters as the main text. The sponges around the ears and below the head are detected and appear dark in T_1 maps and bright in bone enhanced images. Although TE is minimized to 50 μ s to maximize SNR, UTE-MRF loses its sensitivity to short and ultrashort T_2 tissues (Fig. 2). Therefore, the T_2 of sponges and bone is misestimated. There are large T_2 errors at nasal cavity, ventricle, and skull basis especially in sagittal scan. This is highly probably caused by the flow induced signal mismatching in ventricle and the absence of signal in nasal cavity and skull bases.

Supporting Information TABLE S1. The Comparisons between the Nominal Relaxation Times and the Average Measurements from UTE-MRF

(ms)	Muscle	Tendon	Total water	Free water
Nominal T₁	1400	621	246	524
UTE-MRF T₁	1395	619	245	523
Nominal T₂/T₂'/T₂*	32/114/25	3/9.9/2.3	1.2/1.7/0.7	3.5/7.6/2.4
UTE-MRF T₂	32.3	2.6	0.7	3.4